ACTA ACUSTICA UNITED WITH ACUSTICA
Vol. 90 (2004) 49 – 61

Modeling of the Parametric Transmission with the Spatial Fourier Formalism. Optimization of a Parametric Antenna

Jacques Marchal, Pierre Cervenka
Laboratoire de Mécanique Physique associé au CNRS (UMR 7068), Université Pierre et Marie Curie,
2, place de la gare de ceinture, F-78210 Saint-Cyr-l'Ecole, France

Summary
This paper addresses the modeling of parametric transmission by means of the Fourier formalism. This approach is very convenient to understand the influence of the parameters that compete to shape the secondary fields. Non-linear interactions are described with the second order approximation. Finite amplitudes are taken into account. The model can handle a large range of antennae geometry. The secondary field is obtained at any distance of the projector. The effect of diffraction, attenuation and saturation are discussed. A comparison between numerical results and experimental data is shown. Charts have been computed to optimize a parametric antenna.
PACS no. 43.25.Lj

1. Introduction

Several difficulties may arise in the modeling of parametric transmission under actual operating conditions. For instance, the acoustic field of interest can be at any finite distance with respect to the characteristics lengths of the primary field; the source level can be high enough so that the primary waves undergo a significant saturation phenomenon; the primary beam patterns may have a critical effect. This paper overviews the interest of the spatial Fourier formalism to handle these problems. The general model that is built enables to overcome most restrictions on the antenna geometry and the distance of observation. This approach is very convenient to understand the influence of the parameters that compete to shape the secondary fields.

The principle of parametric transmission, and the main ideas that support the developed models in this domain are summarized in section 2. The modeling of parametric antenna by means of the Fourier formalism is fully detailed in section 3. The quasi-linear model and the interactions of finite-amplitude waves are both addressed. Numerical results obtained after these theoretical models are compared with experimental data in section 4. The design of a parametric antenna is addressed in section 5. The typical behavior of the secondary field that is created in the quasi-linear condition is analyzed. The effect of diffraction is discussed. Charts computed with the complete model that takes into account saturation are exhibited. These results show how an optimal choice of parameters can be derived to design parametric antennae.

2. Fundamental in parametric transmission

Since Westervelt released the original principle of the parametric transmission [1], many models have been proposed to describe the radiated fields. Several comprehensive reviews are available, e.g. [2, 3]. The basic principle of the parametric transmission is to transmit simultaneously two primary beams. The non-linear interaction of these fields creates waves at frequencies which are linear combinations of the primary frequencies ω_1 and ω_2. The wave of interest is at the difference frequency $\omega_- = \omega_2 - \omega_1$. Waves at higher frequencies undergo larger viscous attenuation so that they are more likely to vanish at lesser distances of propagation. The main advantage of the parametric transmission is that this so-called secondary field can be a narrow beam, hence obtained with a physical antenna whose size is not very large compared to the corresponding wavelength. Other benefits are the potential large frequency bandwidth reachable with such transmitters, and the low level of the possible sidelobes in the parametric field. However, a significant drawback is the poor efficiency of the non-linear conversion. Unfortunately, increasing the source level leads to a saturation phenomenon that reduces both the parametric gain and directivity. Hence, the design of an efficient transmitter involves a delicate balance of the parameters of the antenna with respect to the required characteristics of the secondary beam.

Within the frame of binary non-linear interactions, the wave equation reads in term of the acoustic potential ϕ,

$$\Box' \phi = S(\phi, \phi). \tag{1}$$

Received 28 June 2002,
accepted 6 October 2003.

The left side of equation (1) is the classical d'Alembertian operator in absorbing media:

$$\Box'(\bullet) = \left(1 + \frac{b}{\rho_0 c_0^2}\frac{\partial^2}{\partial t^2}\right)\nabla^2 \bullet - \frac{1}{c_0^2}\frac{\partial^2 \bullet}{\partial t^2}, \tag{2}$$

where ρ_0, c_0, and b are the fluid density, sound speed, and dissipation coefficient, respectively. Note that the coefficient of linear absorption, α, at a given angular frequency, ω, is related to these parameters via

$$\alpha = \frac{b\omega^2}{2\rho_0 c_0^3}. \tag{3}$$

The right side of equation (1) is a quadratic source term defined by:

$$S(\bullet) = \frac{1}{c_0^2}\frac{\partial}{\partial t}\left(\left(\nabla \bullet\right)^2 + \frac{B}{2A}\frac{1}{c_0^2}\left(\frac{\partial \bullet}{\partial t}\right)^2\right), \tag{4}$$

where $\beta = 1 + B/2A$ is the coefficient of nonlinearity.

In the quasi-linear theory, it is assumed that: 1) the primary waves $\phi_{1,2}$ obey the linear wave equation; 2) the secondary wave ϕ_- is created by the interaction of the only primary waves:

$$\Box'(\phi_{1,2}) = 0, \tag{5}$$

$$\Box'(\phi_-) = S_-(\phi_1, \phi_2). \tag{6}$$

Note that S in equation (4) addresses all combination of frequencies, whereas the source function S_- in equation (6) is restricted to the interaction that yields the difference frequency component.

The many models that are proposed in the quasi-linear theory differ essentially by the way they describe the primary fields and simplify the source distribution that equation (5) implies.

The Westervelt model exemplifies the principle of the parametric transmission (Figure 1a). The source volume is in fine interpreted as an end-fire array whose length is only limited by the linear absorption. Such geometry yields a beam pattern that is devoid of side-lobe. In addition, the directivity is proportional to the square root of the array length. An approximation of the half-power angular aperture in the farfield is

$$2\theta_W = \frac{2}{\sqrt{\pi}}\sqrt{\frac{\lambda_-}{l_a}} \tag{7}$$

where λ_- is the secondary wavelength; the virtual array length is commensurate to the absorption distance defined by:

$$l_a = \alpha^{-1} \quad \text{with} \quad \alpha = \alpha_1 + \alpha_2 - \alpha_-. \tag{8}$$

The Westervelt model emphasizes the role of linear attenuation. Because the primary field is described by collimated plane waves, the implicit hypothesis is that the whole source volume is located in the primary nearfield.

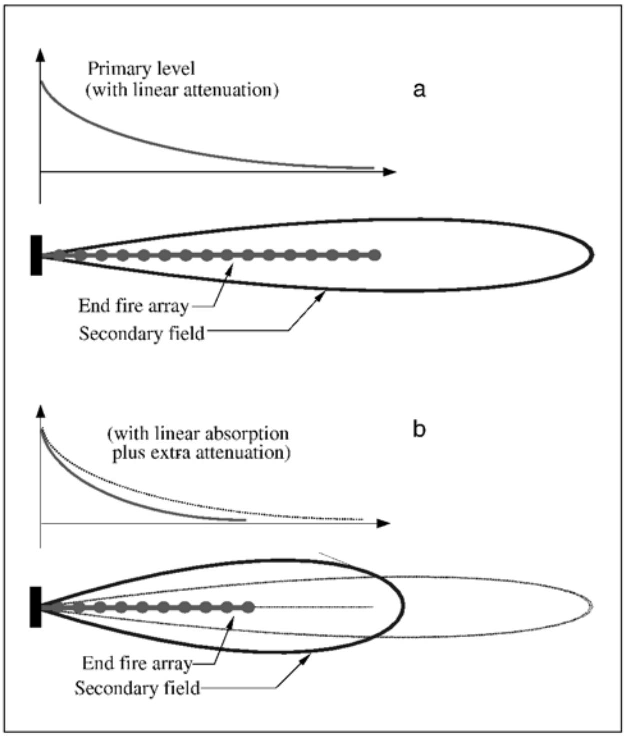

Figure 1. a: Scheme of the Westervelt model. b: Interpretation through the Westervelt model of the effect of saturation.

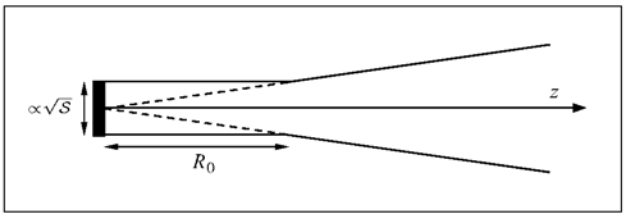

Figure 2. Example of a composite source volume model.

The validity of this model depends on the size of the antenna. The Rayleigh length gives the typical distance of the transition between the nearfield and the farfield:

$$R_0 = \mathcal{S}\lambda_{1,2}. \tag{9}$$

In the Westervelt model, the surface of the antenna, $\mathcal{S}$, must be large enough so that the relationship $l_a < R_0$ holds. An extreme opposite situation occurs when $l_a \gg R_0$: Primary fields diverge, and the source volume is modeled with a cone [4]. Intermediate configurations have been also largely studied, e.g. [5, 6, 7]. For example, the nearfield portion involves plane, collimated waves, and the remaining part is described with spherical waves (Figure 2).

Besides the linear attenuation and the shape of the antenna, saturation is the third main factor that can play an important role. In that case, the hierarchy that equations (5), (6) impose is no longer valid. The only global equation (1) must apply. The characteristic length for saturation is the shock formation distance,

$$l_s = \frac{c_0}{\beta \omega_{1,2} M}, \tag{10}$$

where M denotes the Mach number. The Gol'dberg number characterizes the relative influence of saturation versus linear absorption,

$$\Gamma = l_a / l_s. \tag{11}$$

Note that the Westervelt model provides also a very intuitive picture of the effects of saturation: As the primary level increases ($\Gamma > 1$), the temporal spectral spreading induces an extra-attenuation that reduces the relative length of the end fire array. Consequently the secondary beam pattern broadens (Figure 1b).

Actually, equation (1) cannot be handled directly. The current approach is to consider that most part of the field at the difference frequency is created by the interaction of the only primary waves, i.e. equation (6) still applies. However, the finite amplitude of the primary waves must be taken into account. The extra-attenuation can be evaluated by solving the global equation (1) in a 1-D model from which the relative evolution of each primary component along the direction of propagation is extracted. For example, Moffett and Mellen [6] use such a method. They introduce a taper function in a description of the source volume that is similar to the scheme depicted in Figure 2, but for a continuous transition between the plane zone and the spherical zone.

The previously mentioned models are based on straightforward assumptions in the source distribution. Other models attempt to refine the description of the primary fields. One way consists of evaluating the primary beams by using Green functions [8]. Numerical simulation can be also built with the finite-difference approach based on the KZK equation [9, 10]. Significant results concern the harmonic generation in sound beams, and the distortion of pulse waves, obtained by means of analysis in the frequency domain [11] and the time domain [12], respectively. Another technique consists of using the spatial Fourier decomposition into plane waves [13, 14]. This formalism is well adapted to analyze the interactions of the primary fields as a secondary source. This latter method is applied in the present paper.

3. Spatial Fourier analysis

3.1. Linear propagation

Let us consider a harmonic acoustic field, $g(\boldsymbol{r}, t) = G(\boldsymbol{r}) \exp(-\mathrm{j}\omega t)$, that propagates linearly in a viscous fluid towards the direction $z > 0$ (notation of coordinates is introduced in Figure 3). There is no source in the half space $z > 0$.

The spatial Fourier analysis breaks the field as a sum of plane waves [15]. The decomposition is performed in

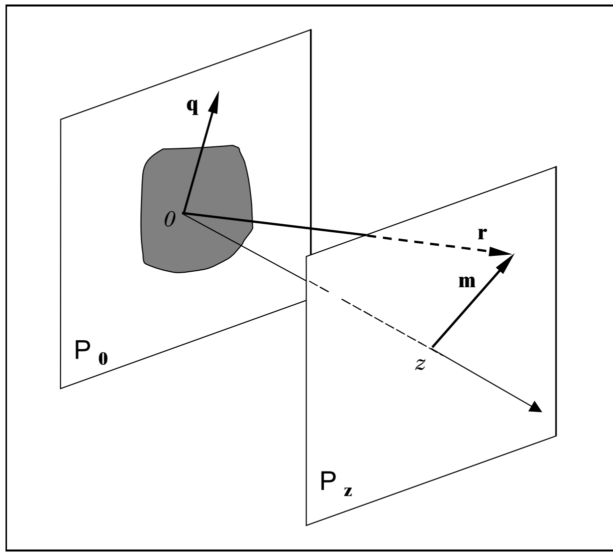

Figure 3. Notation of coordinates with respect to the reference plane.

the reference plane $\Pi_0 (z = 0)$. Let us consider the inhomogeneous plane modes [16], at the angular frequency ω, whose wave vector $\boldsymbol{k}' = \boldsymbol{k} + \mathrm{j}(\alpha/\cos\theta)\boldsymbol{e}_z$ is complex:

$$L_{\omega,\boldsymbol{f}}(r) \exp\left(-\mathrm{j}\omega t\right) = \exp\left(\mathrm{j}\boldsymbol{k}' \cdot \boldsymbol{r}\right) \exp\left(-\mathrm{j}\omega t\right). \tag{12}$$

The real part $\boldsymbol{k}$ of the wave vector $\boldsymbol{k}'$ is such that $k = \omega/c$, $\boldsymbol{k} = k_z \boldsymbol{e}_z + 2\pi \boldsymbol{f}$, and $\sin\theta = 2\pi f/k$ (Figure 4). Vector $\boldsymbol{k}$ makes an angle θ with the z-axis; its component in the reference plane defines the spatial frequency vector $\boldsymbol{f}$; its projection along the z-axis is $k_z = \sqrt{k^2 - 4\pi^2 f^2}$. Taking into account $\alpha/k \ll 1$ and excluding far off-axis modes – i.e. there is no $\cos\theta \ll 1$ – it can checked that the wave vector $\boldsymbol{k}'$ obeys the dispersion law associated with the equation of linear propagation in absorbing media:

$$\left(1 - 2\mathrm{j}\frac{\alpha c_0}{\omega}\right) k'^2 - \frac{\omega^2}{c_0^2} = 0. \tag{13}$$

Equation (12) can be written

$$L_{\omega,\boldsymbol{f}}(\boldsymbol{r} = \boldsymbol{m} + z\boldsymbol{e}_z) = H_z(\omega, f) \exp\left(\mathrm{j}2\pi \boldsymbol{f} \cdot \boldsymbol{m}\right) \tag{14}$$

with

$$H_z(\omega, f) = \exp\left(\mathrm{j}k_z z - \frac{\alpha z}{\cos\theta}\right).$$

$H_z(\omega, f)$ is the linear operator of propagation from plane Π_0 to Π_z. Equation (14) shows that the inhomogeneous plane modes are compatible with the Fourier formalism: Within each plane Π_z parallel to the reference plane Π_0, the signature is harmonic ($2\pi \boldsymbol{f} \cdot \boldsymbol{m}$), and the amplitude is a constant, $|H_z(\omega, f)|$.

Hence, the distribution G of the acoustic field in the reference plane can be expressed by means of the decomposition

$$G(\boldsymbol{q} \in \Pi_0) = \iint A_0(\boldsymbol{f}) \exp\left(\mathrm{j}2\pi \boldsymbol{f} \cdot \boldsymbol{q}\right) \mathrm{d}\boldsymbol{f}. \tag{15}$$

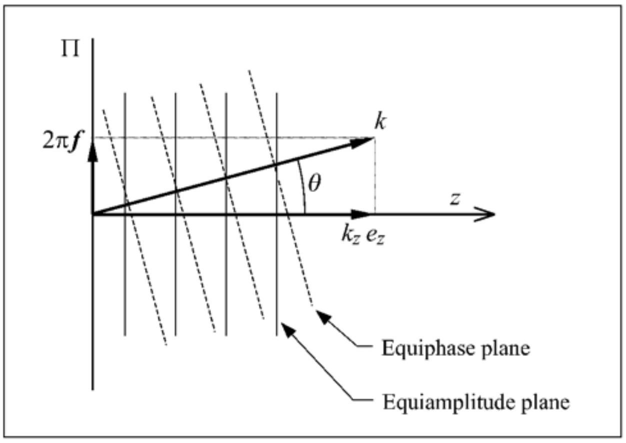

Figure 4. Inhomogeneous plane mode.

The spectrum $A_0(\boldsymbol{f})$ is the spatial Fourier transform of G in Π_0:

$$A_0(\boldsymbol{f}) = \iint_{\Pi_0} G(\boldsymbol{q}) \exp\left(-\mathrm{j}2\pi \boldsymbol{f}\cdot\boldsymbol{q}\right) \mathrm{d}\boldsymbol{q}. \quad (16)$$

The spectrum of G in any plane $\Pi_{z\geq 0}$ is thus obtained with the product

$$A_z(\boldsymbol{f}) = A_0(\boldsymbol{f}) H_z(\omega, f), \quad (17)$$

so that conversely

$$G(\boldsymbol{r} = \boldsymbol{m} + z\boldsymbol{e}_z) = \iint A_z(\boldsymbol{f}) \exp\left(\mathrm{j}2\pi \boldsymbol{f}\cdot\boldsymbol{m}\right) \mathrm{d}\boldsymbol{f}. \quad (18)$$

In order to estimate the farfield, the Fraunhofer approximation yields straightforwardly from the initial spectrum:

$$G(\boldsymbol{r}) = \frac{z}{\mathrm{j}\lambda r^2} \exp\left(\mathrm{j}kr - \alpha r\right) A_0\left(\frac{\boldsymbol{m}}{\lambda r}\right). \quad (19)$$

G represents either the acoustic potential ϕ, pressure p, or the z-component of the velocity v_z. The associated spectra are denoted $A^{(\phi)}$, $A^{(p)}$ and $A^{(v)}$, respectively. The relation between p and ϕ reads at the second order:

$$p = -\rho_0 \frac{\partial \phi}{\partial t} + b\Delta\phi - \frac{\rho_0}{2}\left[(\nabla\phi)^2 - \frac{1}{c_0^2}\left(\frac{\partial\phi}{\partial t}\right)^2\right]. \quad (20)$$

In the paraxial case, the last, second order term can be neglected. In addition, the viscous term can be also omitted because attenuation is negligible over a wavelength like distance ($\alpha/k \ll 1$). Hence, the relation between potential and pressure spectra reduces to:

$$A^{(p)} = \mathrm{j}\rho_0\omega A^{(\phi)}. \quad (21)$$

On the other hand, $\boldsymbol{v} = \mathbf{grad}(\phi)$ so that $v_z = \partial\phi/\partial z$ and

$$A^{(v)} = \mathrm{j}k_z A^{(\phi)}. \quad (22)$$

With a baffled plane antenna, the velocity spectrum is completely defined in the reference plane by the Fourier transform $\mathcal{A}(\boldsymbol{f})$ of the aperture:

$$A^{(v)}(\boldsymbol{f}) = v_0 \mathcal{A}(\boldsymbol{f}), \quad (23)$$

where v_0 is the maximal magnitude of the normal velocity on the surface of the antenna. Notice that $A(\boldsymbol{f})$ may take into account any beam steering or shading of the aperture. With a piston-like transmitter, this function is the mere Fourier transform of the pupil area.

Using equations (21), (22), (23), the Fraunhofer approximation (19) becomes:

$$P(\boldsymbol{r}) = P_0 \frac{\exp(\mathrm{j}kr - \alpha r)}{\mathrm{j}\lambda r} \mathcal{A}\left(\frac{\boldsymbol{m}}{\lambda r}\right), \quad (24)$$

with $P_0 = \rho_0 c_0 v_0$.

3.2. Parametric transmission

With a parametric transmitter, two primary fields at angular frequencies ω_1 and ω_2 are generated by the antenna, which is assumed to be located in the reference plane. The acoustic field in this plane can be represented in terms of potentials with two spectra $A_{0,\omega_1}^{(\phi)}(\boldsymbol{f})$ and $A_{0,\omega_2}^{(\phi)}(\boldsymbol{f})$. Because of the nonlinearity of propagation, the primary spectra no longer follow the simple evolution given by equation (17). Acoustic radiations at linear combination of ω_1 and ω_2 are created. All the corresponding modes interact. With parametric transmission, we are interested in the spectrum corresponding to the wave created at the difference frequency $\omega_- = \omega_2 - \omega_1$.

Using the quasi-linear model (section 3.2.1), the primary waves are assumed not to be altered by the nonlinear interactions so that these fields can still be described with the linear model. In addition, following equation (6), the secondary wave is fed by the interaction of the only primary waves. In that case, the elementary problem reduces to the nonlinear interaction of two inhomogeneous plane waves at frequencies ω_1 and ω_2. It is then straightforward to derive the complete secondary field by integrating over the whole set of interacting pairs of modes. Approximations are derived in the paraxial case in Section 3.2.2, or for large antennas in section 3.2.3.

The finite amplitude case is treated in section 3.2.4 by introducing a taper function in order to describe the evolution of the primary spectra. This taper function is evaluated through a 1D model.

3.2.1. Nonlinear interactions in the quasi-linear approximation

Let us consider the interaction of two modes corresponding to the couples $(\omega_1, \boldsymbol{f}_1)$ and $(\omega_2, \boldsymbol{f}_2)$. Within the frame of the quasi-linear approximation, the primary modes are not altered by saturation (equation 5) so that they can be written:

$$\phi_i = A_{0,\omega_i}^{(\phi)}(\boldsymbol{f}_i) H_z(\omega_i, f_i) \exp\left(\mathrm{j}2\pi \boldsymbol{f}_i\cdot\boldsymbol{m}\right) \exp\left(-\mathrm{j}\omega_i t\right), \quad i = 1, 2. \quad (25)$$

The source term in equation (6) reads:

$$S_{-}(\phi_1,\phi_2)=\frac{1}{c_0^2}\frac{\partial}{\partial t}\left(\nabla\phi_1^*\cdot\nabla\phi_2+\frac{B}{2A}\frac{1}{c_0^2}\frac{\partial\phi_1^*}{\partial t}\frac{\partial\phi_2}{\partial t}\right),\quad(26)$$

that expands into

$$\begin{aligned}\Box'\phi_{-} &= \frac{-\mathrm{j}\omega_{-}}{c_0^2}A^{(\phi)*}_{0,\omega_1}A^{(\phi)}_{0,\omega_2}\left(\boldsymbol{k}_1\cdot\boldsymbol{k}_2+\frac{B}{2A}\frac{\omega_1\omega_2}{c_0^2}\right)\\ &\quad\cdot\exp\left(-\frac{(\alpha_2+\alpha_1)z}{\cos\theta_2}+\mathrm{j}(k_{z2}-k_{z1})z\right)\\ &\quad\cdot\exp\big(\mathrm{j}2\pi(\boldsymbol{f}_2-\boldsymbol{f}_1)\cdot\boldsymbol{m}\big)\exp\big(-\mathrm{j}\omega_{-}t\big). \qquad (27)\end{aligned}$$

Invariance of equation (27) in any plane Π_z implies that the created field can be expressed as the inhomogeneous mode associated to the couple ($\omega_{-}=\omega_2-\omega_1, \boldsymbol{f}_{-}=\boldsymbol{f}_2-\boldsymbol{f}_1$), but with an amplitude $A^{(\phi)}_{0,\omega_-}$ that depends on z:

$$\begin{aligned}\phi_{-} &= A^{(\phi)}_{0,\omega_-}(\boldsymbol{f}_{-},z)H_z(\omega_{-},f_{-})\\ &\quad\cdot\exp\big(\mathrm{j}2\pi\boldsymbol{f}_{-}\cdot\boldsymbol{m}\big)\exp\big(-\mathrm{j}\omega_{-}t\big), \qquad (28)\end{aligned}$$

with $H_z(\omega_{-},f)=\exp(\mathrm{j}k_{z-}z-(\alpha_{-}z/\cos\theta_{-}))$, $k_{-}=\omega_{-}/c_0$, $k_{z-}(\boldsymbol{f}_{-})=k_{-}\cos\theta_{-}$ and $\sin\theta_{-}=2\pi f_{-}/k_{-}$. Note that the evolution of $A^{(\phi)}_{0,\omega_-}(\boldsymbol{f}_{-},z)$ after propagation along a distance commensurate to the wavelength λ_{-} is very slow compared to the z-dependence of $H_z(\omega_{-},f_{-})$. This translates into the following relative orders of magnitude:

$$\left|k^2A\right|\gg\left|k\frac{\partial A}{\partial z}\right|\gg\left|k\frac{\partial^2A}{\partial z^2}\right|. \qquad (29)$$

Hence, after introducing (28) in equation (27), and taking into account the approximations derived from (29), one obtains the first order differential equation:

$$\begin{aligned}\frac{\mathrm{d}A^{(\phi)}_{0,\omega_-}}{\mathrm{d}z} &= -A^{(\phi)*}_{0,\omega_1}A^{(\phi)}_{0,\omega_2}\frac{\omega_1\omega_2}{2c_0^3\cos\theta_{-}}\left(\cos\psi+\frac{B}{2A}\right)\\ &\quad\cdot\exp\big(-(\alpha-\mathrm{j}\Delta k)z\big), \qquad (30)\end{aligned}$$

with $\cos\psi=\boldsymbol{k}_1\cdot\boldsymbol{k}_2/(k_1k_2)$. The global attenuation coefficient is:

$$\alpha=\frac{\alpha_1}{\cos\theta_1}+\frac{\alpha_2}{\cos\theta_2}-\frac{\alpha_{-}}{\cos\theta_{-}}. \qquad (31)$$

$(\Delta\boldsymbol{k})\cdot\boldsymbol{r}$ is the phase difference between the source and the created mode. Actually, this phase mismatch is the fundamental origin of the parametric directivity. The non-linear generation of the secondary wave is a cumulative process that is constructive only if the phase rotation is small. Because $\boldsymbol{f}_{-}=\boldsymbol{f}_2-\boldsymbol{f}_1$, notice that $\Delta\boldsymbol{k}$ is oriented along the z axis (Figure 5):

$$\Delta\boldsymbol{k}=\boldsymbol{k}_2-\boldsymbol{k}_1-\boldsymbol{k}_{-}=\big(k_{z2}-k_{z1}-k_{z-}\big)\boldsymbol{e}_z. \qquad (32)$$

The contribution of both primary modes $(\omega_1,\boldsymbol{f}_1)$ and $(\omega_2,\boldsymbol{f}_2)$ to build $(\omega_{-},\boldsymbol{f}_{-})$ is given by integrating equation (30) along the z-axis from the reference plane up to the observation plane:

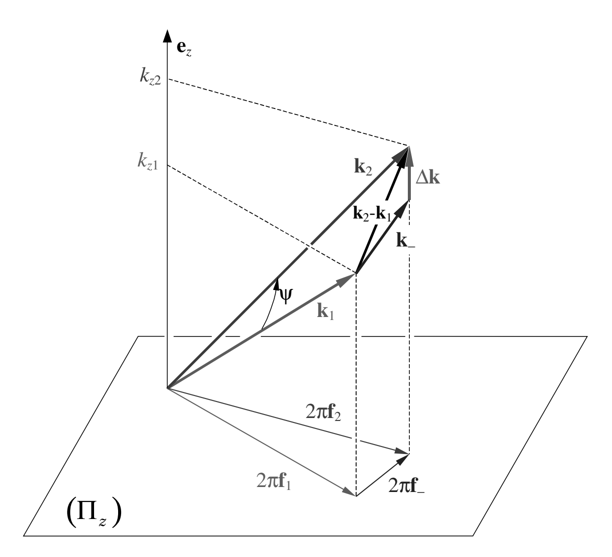

Figure 5. Decomposition of the wave vectors of two interacting modes.

$$A^{(\phi)}_{0,\omega_-}(z,\boldsymbol{f}_{-})=A^{(\phi)*}_{0,\omega_1}(\boldsymbol{f}_1)A^{(\phi)}_{0,\omega_2}(\boldsymbol{f}_2)I(z,\boldsymbol{f}_1\boldsymbol{f}_2), \qquad (33)$$

with

$$\begin{aligned}I(z,\boldsymbol{f}_1\boldsymbol{f}_2) &= -\frac{\omega_1\omega_2}{2c_0^3\cos\theta_{-}}\left(\cos\psi+\frac{B}{2A}\right)\\ &\quad\cdot\frac{1-\exp\big(-(\alpha-\mathrm{j}\Delta k)z\big)}{\alpha-\mathrm{j}\Delta k}. \qquad (34)\end{aligned}$$

At far range, the kernel I does not depend any more on z:

$$I_\infty(\boldsymbol{f}_1\boldsymbol{f}_2)=-\frac{\omega_1\omega_2}{2(\alpha-\mathrm{j}\Delta k)c_0^3\cos\theta_{-}}\left(\cos\psi+\frac{B}{2A}\right). \qquad (35)$$

The phase shift is null ($\Delta k=0$) if and only if the primary wave vectors $\boldsymbol{k}_1$ and $\boldsymbol{k}_2$ are collinear ($\psi=0$, so that $\boldsymbol{k}_{-}=\boldsymbol{k}_2-\boldsymbol{k}_1$). In that case, the nonlinear interaction is fully constructive.

$$I(z,\boldsymbol{f}_{01}\boldsymbol{f}_{02})=-\frac{\beta\omega_1\omega_2(1-\mathrm{e}^{-\alpha z})}{2\alpha c_0^3\cos\theta_{-}}, \qquad (36)$$

with $\boldsymbol{f}_{01}=(\omega_1/\omega_{-})\boldsymbol{f}_{-}$, $\boldsymbol{f}_{02}=(\omega_2/\omega_{-})\boldsymbol{f}_{-}$.

Let us now consider the complete primary field transmitted by an antenna located in the reference plane Π_0. The corresponding primary spectra in that plane are given by $A^{(\phi)}_{0,\omega_1}(\boldsymbol{f})$ and $A^{(\phi)}_{0,\omega_2}(\boldsymbol{f})$. The component at the spatial frequency $\boldsymbol{f}_{-}$ of the secondary spectrum is thus obtained by integrating equation (33) over all the couples $(\boldsymbol{f}_1,\boldsymbol{f}_2=\boldsymbol{f}_1+\boldsymbol{f}_{-})$. The calculation can be centered on the most constructive pair, $(\boldsymbol{f}_{01},\boldsymbol{f}_{02})$, by introducing the new spatial frequency vector $\boldsymbol{f}'$:

$$\begin{aligned}A^{(\phi)}_{0,\omega_-}(z,\boldsymbol{f}_{-}) &= \iint A^{(\phi)*}_{0,\omega_1}(\boldsymbol{f}_{01}+\boldsymbol{f}')A^{(\phi)}_{0,\omega_2}(\boldsymbol{f}_{02}+\boldsymbol{f}')\\ &\quad\cdot I(z,\boldsymbol{f}_{01}+\boldsymbol{f}',\boldsymbol{f}_{02}+\boldsymbol{f}')\,\mathrm{d}\boldsymbol{f}', \qquad (37)\end{aligned}$$

with

$$\boldsymbol{f}' = \boldsymbol{f}_1 - \boldsymbol{f}_{01} = \boldsymbol{f}_2 - \boldsymbol{f}_{02} = (\omega_2 \boldsymbol{f}_1 - \omega_1 \boldsymbol{f}_2)/\omega_-. \tag{38}$$

Note that $A^{(\phi)}_{0,\omega_-}(z, \boldsymbol{f}_-)$ is the spectrum that corresponds to the secondary field built in the plane Π_z. However, this spectrum is referenced in the plane Π_0. The secondary field in the plane Π_z is thus obtained with:

$$\Phi_-(\boldsymbol{r}) = \iint A^{(\phi)}_{0,\omega_-}(z, \boldsymbol{f}_-) H_z(\omega_-, f_-) \cdot \exp\big(-\mathrm{j}2\pi \boldsymbol{f}_- \cdot \boldsymbol{m}\big)\, \mathrm{d}\boldsymbol{f}_-. \tag{39}$$

In the farfield, the Fraunhofer approximation (19) applies with the spectrum (37). Hence, it gives directly the field without needing any inverse Fourier transform.

There are several advantages in using the Fourier formalism to model parametric transmission. From a practical point of view, the numerical implementation of equation (37) is eased because the domain of integration that gives a significant contribution is limited around $(\boldsymbol{f}_{01}, \boldsymbol{f}_{02})$ and its extend can be readily monitored with equation (34). In addition, the only requirement concerning the description of the primary fields is that the initial spectra can be defined in the reference plane: it allows to consider many antenna settings, e.g. any plane or quasi-plane geometry, taking also into account beamsteering and aperture shadowing. However, the main interest of the Fourier analysis is that the source volume is modeled exactly. There is no need to delimit several particular regions of space, e.g. nearfield with plane waves and farfield with spherical waves. Furthermore, the primary and secondary fields can be obtained at any distance of the reference plane.

3.2.2. Paraxial approximation

In the paraxial case, i.e. when primary waves are directive enough along the z axis, two approximations can be used in evaluating the kernel function: 1) The angular dependences can be withdrawn from amplitude terms ($\cos\theta_i \approx 1$); 2) The second order development of Δk applies to evaluate the phase term:

$$I(z, f') = -\frac{\beta\omega_1\omega_2}{2c_0^3} \frac{1 - \exp\big(-(\alpha - \mathrm{j}\Delta k)z\big)}{\alpha - \mathrm{j}\Delta k}, \tag{40}$$

with $\quad \alpha = \alpha_1 + \alpha_2 - \alpha_-$

and $\quad \Delta k = \Delta k(f') = \dfrac{2\pi^2 c_0 \omega_-}{\omega_1\omega_2} f'^2. \quad (41)$

Considering a plane, baffled antenna in the paraxial case, the secondary pressure spectrum is:

$$A^{(p)}_{0,\omega_-}(z, \boldsymbol{f}_-) = -\mathrm{j}\frac{P^*_{01}P_{02}\beta\omega_-}{2\rho_0 c_0^3} \cdot \iint \mathcal{A}^*_1(\boldsymbol{f}_{01} + \boldsymbol{f}')\mathcal{A}_2(\boldsymbol{f}_{02} + \boldsymbol{f}') \cdot \frac{1 - \exp\big(-(\alpha - \mathrm{j}\Delta k(f'))z\big)}{\alpha - \mathrm{j}\Delta k(f')}\, \mathrm{d}\boldsymbol{f}', \tag{42}$$

where $P_{0i} = \rho_0 c_0 v_{0i}$ $(i = 1, 2)$ are the equivalent pressures at the antenna surface for each primary radiation, and $(\alpha - \mathrm{j}\Delta k(f'))$ is given by equation (41).

In the farfield, using equations (24), (41), (42), the Fraunhofer approximation reduces into:

$$P_-(\boldsymbol{r}) = -\frac{P_{01}P_{02}\beta\omega_-^2}{4\pi\rho_0 c_0^4} \frac{\exp(\mathrm{j}k_- r - \alpha_- r)}{r} \cdot \iint \mathcal{A}^*_1\Big(\frac{\boldsymbol{m}}{\lambda_1 r} + \boldsymbol{f}'\Big)\mathcal{A}_2\Big(\frac{\boldsymbol{m}}{\lambda_2 r} + \boldsymbol{f}'\Big) \cdot \frac{1}{\alpha - \mathrm{j}\Delta k(f')}\, \mathrm{d}\boldsymbol{f}'. \tag{43}$$

3.2.3. Large antenna approximation

Equation (43) can be linked to the Westervelt [1] and Naze-Tjotta [17] models in case of large antennas. Elements of the rigorous calculus can be found in [8] for circular projector, or in [18] (Part C.2). The roadmap of the derivation is only recalled here.

The larger is the antenna, the narrower are the primary spectra $\mathcal{A}$. Whenever the condition

$$\alpha R_0 \omega_{1,2}/\omega_- \gg 1 \tag{44}$$

is met, the kernel $1/a_-$ in the integrand of equation (43) can be considered as constant within the domain of integration that the product of the spectra $\mathcal{A}^*_1\mathcal{A}_2$ dictates. This domain is centered on the spatial frequency $\boldsymbol{f}'_0 \approx -\boldsymbol{m}/(\lambda_{1,2} r)$. Consequently, the secondary farfield pressure induced by a piston-like baffled antenna reduces to:

$$|P_-(r)| = P_W(r) D_W(\theta) D_A(\boldsymbol{\theta}), \tag{45}$$

with $\boldsymbol{\theta} = \boldsymbol{m}/r$, where P_W denotes the Westervelt on-axis pressure:

$$P_W(r) = \frac{P_{01}P_{02}\,\mathcal{S}\,\beta\omega_-^2}{4\pi\rho_0\alpha c_0^4} \frac{\exp(-\alpha_- r)}{r}, \tag{46}$$

D_W is the Westervelt directivity (related to equation (7) with $\theta_W^2 = 2\alpha/k_-$):

$$D_W(\theta) = \frac{\alpha}{|\alpha - \mathrm{j}\Delta k(f'_0)|} = \left|1 - \mathrm{j}\frac{\theta^2}{\theta_W^2}\right|, \tag{47}$$

and $D_A(\boldsymbol{\theta})$ is the directivity function associated to the projector directly driven at the difference frequency:

$$D_A(\boldsymbol{\theta}) = \frac{1}{\mathcal{S}} \iint \mathcal{A}^*_1\Big(\frac{\boldsymbol{m}}{\lambda_1 r} + \boldsymbol{f}'\Big)\mathcal{A}_2\Big(\frac{\boldsymbol{m}}{\lambda_2 r} + \boldsymbol{f}'\Big)\, \mathrm{d}\boldsymbol{f}' = \frac{1}{\mathcal{S}}\mathcal{A}(\boldsymbol{\theta}/\lambda_-). \tag{48}$$

3.2.4. Finite-amplitude interactions

Writing equation (1) with the Fourier formalism would involve a huge number of spatial spectra, $A_{0,p\omega_1+q\omega_2}(z, \boldsymbol{f})$, whose corresponding modes interact each other. At the present state of the computer capabilities, the computational management induced by such an approach would not be reasonable.

In order to reduce the complexity of the problem, the proposed model is based on the assumption that most of the secondary field is created by the only interaction of the primary waves, i.e. equation (6) applies. However, the finite amplitude of the primary waves is taken into account by introducing in equation (27) a z-dependence of the spectra $A_{0,\omega_1}(z,\boldsymbol{f})$ and $A_{0,\omega_2}(z,\boldsymbol{f})$.

On the other hand, because one major interest of parametric transmission is to produce a narrow beam, the antenna must be designed to generate reasonably directive primary beams. In that case, most of the contribution to build the secondary field comes from the paraxial primary modes. Consequently, the primary spectra used in equation (6) to evaluate the secondary field are modeled by separating the variables z and $\boldsymbol{f}$. Considering for now only plane antennae, one uses the notations:

$$A^{(v)}_{0,\omega_i}(z,\boldsymbol{f}) = u_i(z)A_{0i}(\boldsymbol{f}), \quad i = 1,2. \tag{49}$$

The taper functions $u_i(z)$ are dimensioned in terms of acoustic velocities. The ratios $u_i(z)/v_{0i}$ represent the extra-attenuation that the saturation effect introduces in the primary waves. Equation (49) implies that the primary fields are described, in any plane Π_z, with the same relative distributions as in the linear case. The underlying assumption is that the prominent effect of saturation in the building of the secondary field is the relative shortening of the source volume, rather than the alteration in its lateral distribution.

Let us denote the acoustic velocities $v_i(z) = u_i(z)\exp(-\alpha_i z)$, which take into account the overall attenuation, i.e. linear absorption plus extra-attenuation. These functions are derived by solving equation (1) in a 1D model. Because waves are created at the linear combination of the primary frequencies, it is convenient to adopt a notation with two indexes. The indexed quantity $X_{i,j}$ refers to the component at frequency $\omega_{i,j} = i\omega_1 + j\omega_2$ (> 0). The relation with the former notation is thus: $X_{1,0} = X_1$, $X_{0,1} = X_2$ and $X_{-1,1} = X_-$. Equation (1) translates into the set of differential equations:

$$\begin{aligned}\frac{\mathrm{d}v_{m,n}}{\mathrm{d}z} &= -\alpha_{m,n}v_{m,n} \\ &+ \mathrm{j}\omega_{m,n}\frac{\beta}{2c_0^2}\Bigg\{\frac{1}{2}\sum_{i+k=m}\sum_{j+l=n} v_{i,j}v_{k,l} \\ &\qquad - \sum_{i-k=m}\sum_{j-l=n} v_{i,j}v^*_{k,l}\Bigg\},\end{aligned} \tag{50}$$

with the initial conditions: $v_{1,0}(0) = u_{1,0}(0) = v_{01}$, $v_{0,1}(0) = u_{0,1}(0) = v_{02}$, all other $v_{i,j}(0)$ being null.

Using equation (49), equation (42) is modified into:

$$\begin{aligned}A^{(p)}_{0,\omega_-}(z,\boldsymbol{f}_-) = \mathrm{j}\frac{\beta\rho_0\omega_-}{2c_0}\iint &\mathcal{A}_1^*(\boldsymbol{f}_{01}+\boldsymbol{f}') \\ &\cdot \mathcal{A}_2(\boldsymbol{f}_{02}+\boldsymbol{f}')K(z,f')\,\mathrm{d}\boldsymbol{f}',\end{aligned} \tag{51}$$

with the kernel:

$$\begin{aligned}K(z,f') = \int_0^z &v_1^*(z)v_2(z) \\ &\cdot \exp\Big(-\big(\alpha - \mathrm{j}\Delta k(f')\big)z\Big)\,\mathrm{d}z,\end{aligned} \tag{52}$$

where $\alpha - \mathrm{j}\Delta k(f')$ is defined in equation (41).

By taking $u_i(z) = v_{0i}$, it can be checked that equation (51) reduces to the solution (42) corresponding to the quasi-linear model in the paraxial case. Note also that there is in that case

$$I(z,f') = -\frac{\omega_1\omega_2\beta}{2c_0^3}K(z,f').$$

According to equation (39), the field is obtained at any finite distance by means of the inverse Fourier transform of the spectrum (51):

$$\begin{aligned}P_-(\boldsymbol{r}) = \iint &A^{(p)}_{0,\omega_-}(z,\boldsymbol{f}_-)H_z(\omega_-,f_-) \\ &\cdot \exp(-\mathrm{j}2\pi\boldsymbol{f}_-\cdot\boldsymbol{m})\,\mathrm{d}\boldsymbol{f}_-,\end{aligned} \tag{53}$$

The farfield is directly computed with the Fraunhofer approximation (19):

$$\big|P_-(\boldsymbol{r})\big| = \frac{\exp(-\alpha r)}{\lambda_- r}\left|A^{(p)}_{0,\omega_-}\Big(\frac{\boldsymbol{m}}{\lambda r}\Big)\right|. \tag{54}$$

4. Numerical model and comparison with experimental results

4.1. Numerical model

A software tool has been developed to implement the model described in the previous section. Source levels are input to derive the extra-attenuation by means of the 1-D set of equations (50); primary spectra (49) can describe rectangular and circular apertures; the secondary spectrum is evaluated with the integral (51); the secondary field is obtained at finite distances with an inverse 2-D Fourier transform (for circular transmitter, the computing is simplified because it requires a simple, 1-D Fourier-Bessel transform, as in equation 53); parametric farfields of rectangular or circular antennas are calculated with equation (54).

Notice that the most time consuming operation is the calculation of the secondary spectrum by equation (51) because it involves a 2-D integration. However, the kernel $K(z,f')$, given by equation (52), is tabulated along f', and the extent of the significant spatial frequency domain is asserted. Consequently, the integration of the product of the primary spectra can be conveniently monitored with this kernel.

Environment parameters are derived from empirical models: Sound speed and attenuation are computed with the Lovett [19] and François-Garrison [20] formulas, respectively. They are reproduced in the Appendix.

4.2. Comparison with experiments

Results obtained with the numerical model are compared with experimental data. Three sets of measurements performed with circular piston projectors are presented. The first set comes from an experiment made by Muir and Willette [4]. The second set comes from the investigation of Garrett *et al.* [21, 22, 23]. The third experiment has been carried with a projector built in our laboratory [24]. The main characteristics of these tests are summarized in Table I.

Muir and Willette performed their measurements in fresh water. The Rayleigh distance is much smaller than the absorption length. Consequently, the difference-frequency generation is dominated by nonlinear interactions in the farfield of the primary beams. Muir and Willette proposed a quasi-linear theoretical model that is suited to such geometry. The mean source level is 204 dB ref 1μPa rms at 1 m, so that the Gol'dberg number is about $\Gamma = 8$. With such figures, the hypothesis that the primary fields obey the linear wave equation seems questionable. However, the spherical spreading reduces the effect of the saturation induced losses, and the validity of the quasi-linear approach is confirmed with the results obtained by these authors (Figure 6). The parameters of this experiment have been used to compute the secondary spectrum with our model (51), at $z = 38$ m. The secondary field has been directly derived from the spectral values with the Fraunhofer approximation (54). These numerical results are plotted in Figure 6. The superimposition with experimental data exhibits a good agreement.

With the experiment of Garrett *et al.*, the secondary field is observed in the nearfield of the primary beams. Several parameters of the experiment are not readily available. However, our numerical simulation shows that the secondary beam pattern does not depend significantly on the estimated parameters (e.g. temperature), so that a comparison can be performed. In addition, the on axis level is not of concern because of the quasi-linear condition (the observation distance is much smaller than the shock formation distance). On the other hand, experimental data were already faced with the theoretical results in the nearfield derived by Naze-Tjotta and Tjotta [25, 26, 27]. Figure 7 reproduces this comparison, together with our numerical simulation. Here again, a good agreement is observed.

A circular antenna has been built in our laboratory (70 cm diameter, 100 kHz central frequency). Measurements are performed at a few tens meters range in the GESMA (Groupe d'Etudes Sous-Marines de l'Atlantique) tank facility. The difference frequency varies from 10 kHz up to 30 kHz. The influence of the transmitting power level is also observed (215 to 230 dB ref 1μPa rms at 1 m).

Compared to the above-mentioned experiments, the Rayleigh distance is half way between the projector and the measurement location. The parametric beam is not yet fully developed at this distance because both the absorption distance and the shock formation distance are larger. Hence the observed secondary field results from non-linear interactions that occur both in the nearfield and

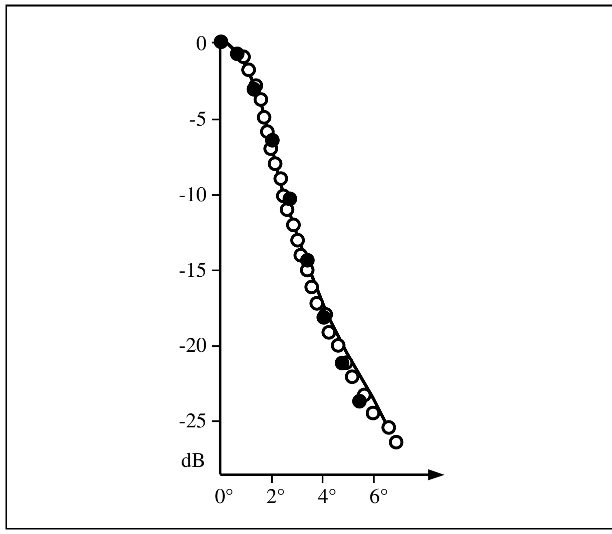

Figure 6. Beam pattern produced by a parametric array. Empty circle: Muir and Willette experimental data [4]; Solid line: Muir and Willette numerical results [4]; Solid circle: Numerical results with Fourier based analysis.

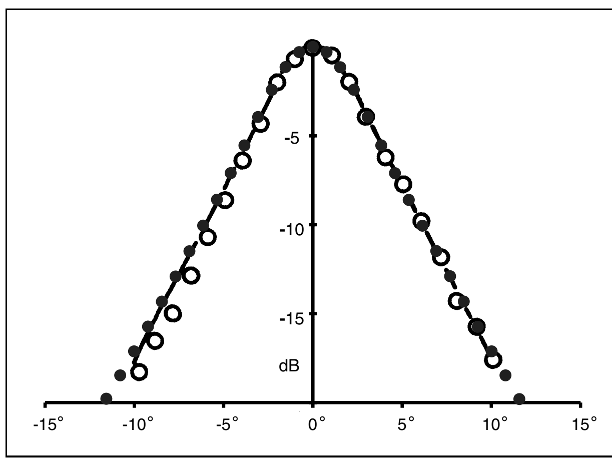

Figure 7. Beam pattern produced by a parametric array. Empty circle: Garrett *et al.* experimental data [22]; Solid line: Garrett *et al.* numerical results [22]; Solid circle: Numerical results with Fourier based analysis.

in the transition zone of the primary beams. The secondary spectra corresponding to the experimental settings are computed with equation (51), at $z = 59$ m. The width θ_- of these spectra imply equivalent Rayleigh lengths $\lambda_-/(\theta_-)^2$ that are much larger than z. It forbids to derive straightforwardly the pressure field with the Fraunhofer approximation. Consequently, the inverse Fourier-Bessel transform have been applied to obtain the results displayed in Figure 8. Theoretical and experimental results match closely.

At 100 kHz, the primary beamwidth is 1.3° at -3 dB. Driven directly at the difference frequency, this projector would produce beamwidths of 4.3°, 6.4° and 12.8°, at 30 kHz, 20 kHz and 10 kHz, respectively. Accordingly, sidelobes would appear at a relative level of -17 dB in a classical linear transmitting mode. In the cases that

Table I. Characteristics of experiments.

	Projector 1	Projector 2	Projector 3
Diameter	7.6 cm	176 cm	70 cm
Mean Primary Frequency	450 kHz	13 kHz	100 kHz
Difference Frequency	64 kHz	2 kHz	10–20–30 kHz
Rayleigh length	1.4 m	21 m	26 m
Absorption distance	160 m	>10 km	230 m
Shock formation distance	20 m	≈500 m	130 m to 500 m
Distance of observation	38 m	16.9 m	59 m

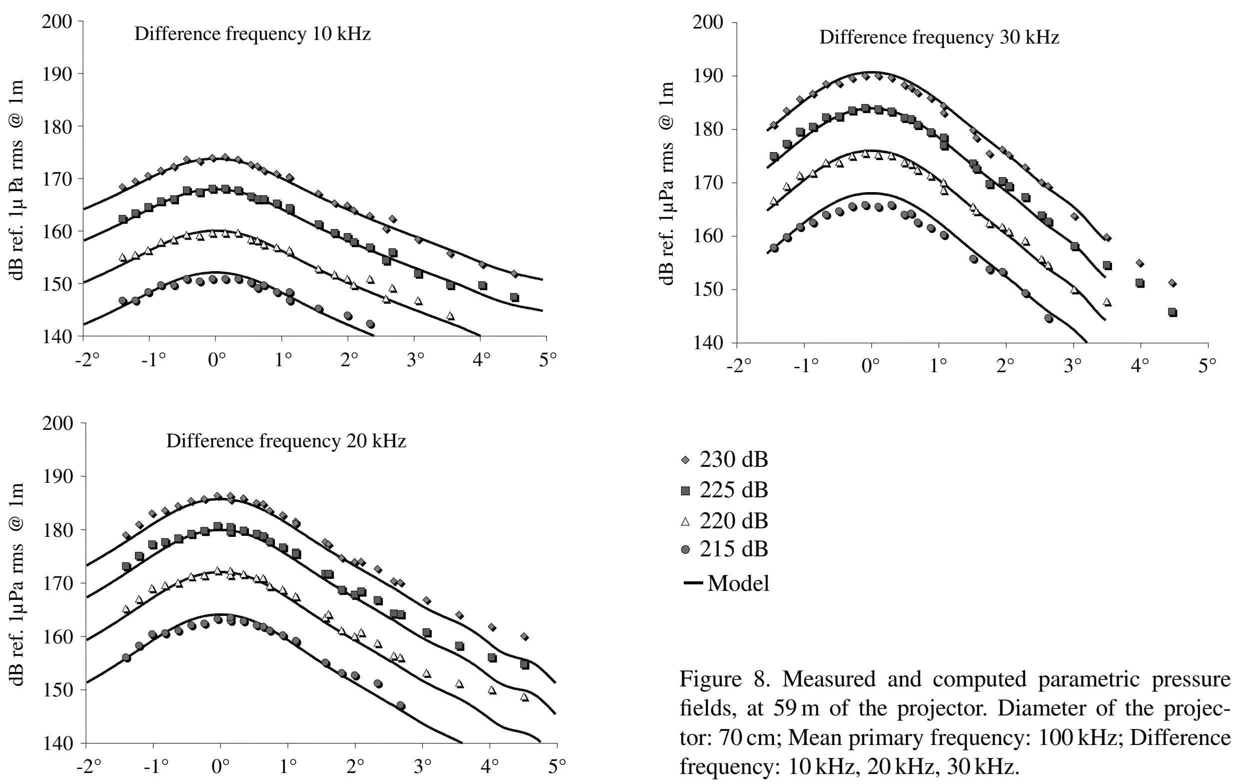

Figure 8. Measured and computed parametric pressure fields, at 59 m of the projector. Diameter of the projector: 70 cm; Mean primary frequency: 100 kHz; Difference frequency: 10 kHz, 20 kHz, 30 kHz.

have been investigated, the parametric beamwidth is in the range 1.5°–1.8°, and no sidelobe has been observed.

5. Behavior of parametric antennas

5.1. Typical Responses in the Quasi-Linear Model

The quasi-linear model is convenient to explore the typical behavior of the secondary field. The aim of this approach is to extract some clues about the effects of the parameters that define a parametric transmitter. A case study is investigated with the above-described theoretical and numerical tools. One chooses a square antenna (side = 50 cm). The difference frequency is also fixed (15 kHz). In order to remain in the hypothesis of the quasi-linear model, the pressure at the surface is 1000 Pa. The mean primary frequencies range from 35 kHz up to 900 kHz. The upper limit extends far beyond a value of practical interest with regard to the size of the antenna (in terms of primary wavelengths): The purpose is to examine the limit case of very large antenna.

Figure 9 displays farfield results obtained with three models: 1) The Fourier based analysis equation (43) which is considered here as the exact solution; 2) The Westervelt evaluations built with equations (7) and (46); 3) The Naze-Tjotta model, equation (45), which introduces the aperture factor (48) in the Westervelt model to correct the beamwidth. Note that according to Eq.(44), the domain of validity of the two latter approximations is restricted to primary frequencies larger than about 100 kHz, although Figure 9 displays the computed values over the whole trial set [35 kHz, 900 kHz].

The bold solid curve shows clearly that an optimal choice of primary frequency exists. This best configuration is reached here when the mean value is around 90 kHz. At a lower primary-to-secondary frequencies ratio, the evolution of the secondary beamwidth departs frankly from the approximate solutions. On the other hand, there is a

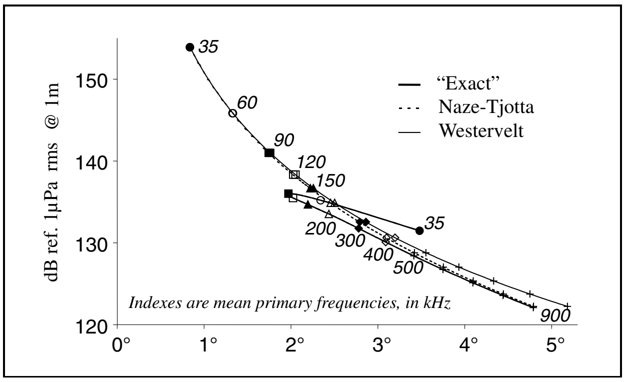

Figure 9. Theoretical parametric level versus beamwidth (at −3 dB). Square projector (side = 0.5 m); 15 kHz difference frequency; 10^3 Pa pressure amplitude at the surface of the projector, for each primary wave. Mean primary frequency varies from 35 kHz up to 900 kHz. Validity of the Westervelt and Naze-Tjotta models starts at primary frequencies larger than 100 kHz.

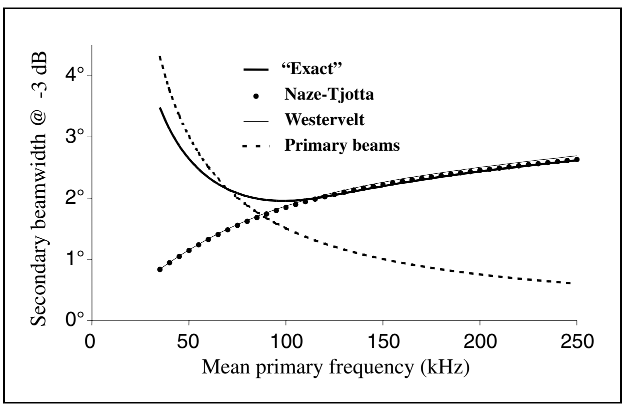

Figure 10. Parametric beamwidth (at −3 dB) versus mean primary frequency. Square projector (side = 0.5 m); 15 kHz difference frequency.

reasonable agreement between all estimates for frequency ratios larger than optimal.

It can be also noticed that the original and modified Westervelt solutions remain close. Actually, a significant difference would only appear for very high primary frequencies. In this unrealistic situation, the parametric aperture tends to the limit dictated by the aperture that the projector would produce if directly driven at the difference frequency (the asymptotic solution is here about 10°). Such parametric transmitter would be indeed useless.

The optimal set of parameters results from two phenomena that compete in building the parametric directivity: 1) given the difference wavelength, the end fire array length increases when the primary frequency decreases (lower attenuation), hence reducing the parametric beamwidth; 2) given the size of the antenna, the primary beamwidth enlarges when the primary frequency decreases. The interaction of the primary waves is constructive within this aperture. Hence, the lower bound of the parametric beamwidth is commensurate to the primary beamwidth. Figure 10 displays the evolution of the directivity obtained with the previously presented models (Figure 9). In addition, the aperture of the primary beam is superimposed. Note that as in Figure 9, mean primary frequencies below 100 kHz are beyond the domain of validity of the Westervelt and Naze-Tjotta models.

The diffraction of the primary waves below 90 kHz dictates the enlargement of the parametric aperture. The end-fire array directivity is predominant beyond this value. As a rule of thumb, the optimal parameters can be approached by equaling the Westervelt aperture and the primary aperture. The existence of such an optimal situation is also outlined in [2, chapter 6] where the theoretical developments are based on primary fields modeled as Gaussian beams. However, although analytical formulas can be derived in some particular configurations, a complete numerical model must be used to estimate the actual performance of an antenna, i.e. the width and level of the parametric field.

5.2. Optimization of a projector

Let us consider again that the fixed parameters are the size of the projector and the difference frequency. The existence of an optimal mean primary frequency that minimizes the parametric aperture has been put in evidence in the previous section. The problem was addressed in the quasi-linear model, so that the source level had no influence on the directivities. Actually, the source level changes the figures when it involves saturation: As described with the Westervelt scheme in Figure 1b, the relative length of the end fire array is reduced when the shock formation distance is smaller than the attenuation length ($\Gamma > 1$). Consequently, the parametric aperture broadens. Because the optimal configuration occurs when the Westervelt angle and the primary beamwidth are close, it can be expected that the mean primary frequency must be lowered with increasing source levels.

Figure 11 is built with a circular projector of radius 1.05 m [28]. It displays the level and the half power beamwidth of the secondary farfield for a variety of source levels and ratios of primary-to-secondary frequencies. The mean primary frequency is scanned from 35 kHz to 85 kHz (step 5 kHz). The source pressure counted at the surface ranges from 1 kPa to 75 kPa.

The lower part of the chart is representative of the asymptotic behavior corresponding to quasi-linear model: The angular response is independent of the source level (solid lines are vertical); the optimal frequency is indeed a constant; the secondary level is proportional to the square of the primary pressure.

The upper part exhibits the effect of saturation: The secondary beamwidth enlarges with the primary level; the secondary level does not grow any more as much as the square of the primary pressure. The array of solid lines is twisted: As expected, the primary frequency that gives the better parametric directivity decreases as the source level increases.

Given a diameter and a secondary frequency, the envelope of Figure 11 gives the best combination of secondary directivity and level. Figure 12 is a collection

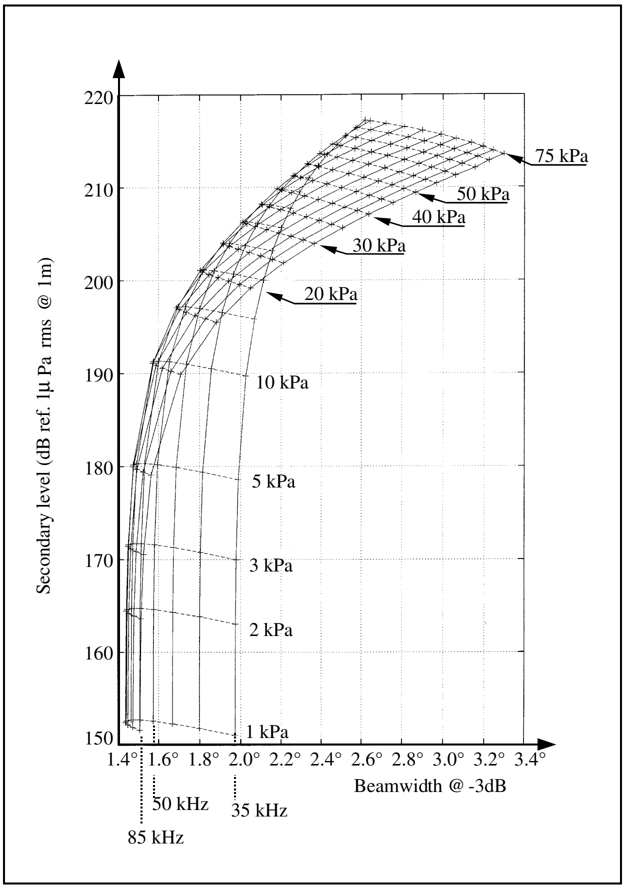

Figure 11. Secondary farfield level versus directivity. Difference frequency: 15 kHz; Diameter of the projector: 1.05 m. Parameters are the mean primary frequency (35 kHz to 85 kHz) and the pressure at the surface of the projector (1 kPa to 75 kPa).

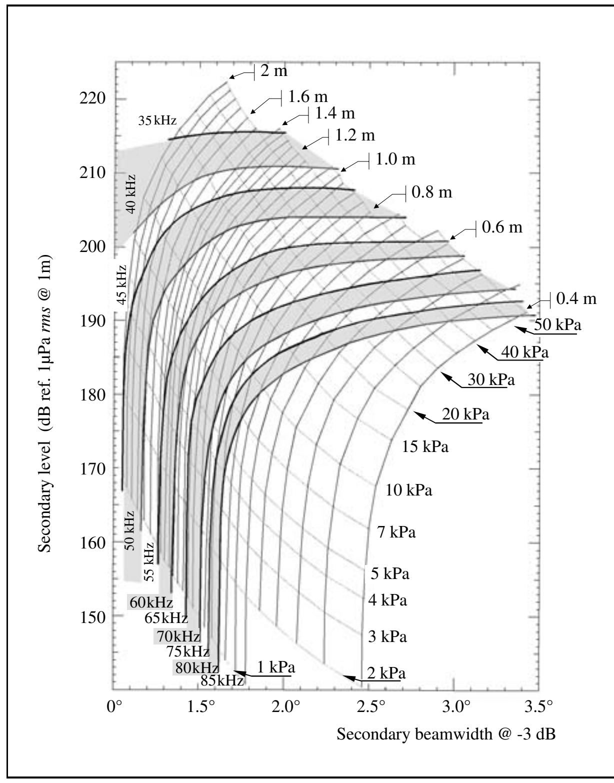

Figure 12. Optimal secondary beam characteristics achievable at 15 kHz difference frequency, with projector diameters ranging from 0.4 m to 2 m. Corresponding primary frequencies and levels.

of such envelopes for various circular projectors. Hence, this chart gives at a glance all the farfield performances (beamwidth and level) that are reachable at 15 kHz difference frequency, together with the parameters to achieve them (diameter of the projector, primary frequencies and level). For example, let us assume that the required width and level of the parametric farfield are 2° and 190 dB ref 1 μPa rms at 1 m, respectively. The chart gives the suitable configuration: 75 cm diameter projector; 70 kHz mean primary frequency (i.e. 62.5 kHz and 77.5 kHz); 17 kPa pressure amplitude at the surface, for each primary wave, i.e. 228 dB ref 1 μPa rms at 1 m source level.

6. Conclusion

The spatial Fourier formalism is a convenient tool to model the paraxial parametric transmission in the frame of nonlinear interactions between finite-amplitude waves. The secondary field can be obtained at finite distances, with versatile projector geometries. The numerical implementation of the theoretical model is manageable with reasonable efforts. Confrontations with experimental data show good agreements.

However, the most questionable hypothesis in the finite-amplitude model is the separability of the distance and spatial frequencies that equation (49) involves. More specifically, the pending question is the limit of validity and the consistency of the 1-D model in estimating the extra-attenuation. Further comparisons with experiments that involve stronger source levels must be performed.

In designing a parametric antenna, a proper balance must be set between the length of the interaction zone and the aperture of the primary beams. In the frame of the quasi-linear assumption, orders of magnitude are easily obtained by simple calculus derived from the Westervelt model and from the approximate width of the field that an antenna generates after linear propagation. However, the complete numerical model cannot be avoided to compute the optimal parameters to be used in the actual situations that involve finite-amplitude interactions. To do so, charts such as presented in Figure 12 can be drawn for any required particular applications, e.g. at finite distances.

Appendix

This appendix contains the formulae for sound speed and absorption that are used to compute the numerical results presented in this paper. The following notations are defined:

z (m): Depth; T (°C): Temperature [-2 °C, $+35$°C];

P (Pa): Pressure referenced from surface, derived from

depth z [0 m, 8000 m] and latitude ϕ by the simplified Leroy's equation $P = 1.0052405 \cdot 10^4(1 + 5.28 \cdot 10^{-3}\sin^2\phi)z + 2.36 \cdot 10^{-2}z^2$.
S: Salinity [0, $42 \cdot 10^{-3}$]; f: Frequency (Hz)

Lovett's model for sound speed:

$$\begin{aligned} c &= c_0 + c_T + c_S + c_P + c_{TSP}, \\ c_0 &= 1402.394, \\ c_T &= 5.01132T - 5.513036 \cdot 10^{-2}T^2 \\ &\quad + 2.221008 \cdot 10^{-4}T^3, \\ c_S &= 1.332947 \cdot 10^3 S \\ c_P &= 1.605336 \cdot 10^{-6}P + 2.12448 \cdot 10^{-15}P^2, \\ c_{TSP} &= -12.66383TS + 9.543664 \cdot 10^{-2}T^2S \\ &\quad - 1.052396 \cdot 10^{-16}TP^2 + 2.183988 \cdot 10^{-25}TP^3 \\ &\quad - 2.253828 \cdot 10^{-22}SP^3 + 2.062107 \cdot 10^{-6}TS^2P. \end{aligned}$$

François and Garrison's model for sound absorption:

$$\alpha = A_0 f^2 + A_1 \frac{f_1 f^2}{f^2 + f_1^2} + A_2 \frac{f_2 f^2}{f^2 + f_2^2}.$$

Fresh water contribution

$T < 20\,°\mathrm{C}$:

$$\begin{aligned} A_0 = &\big(4.937 \cdot 10^{-10} - 2.59 \cdot 10^{-11}T + 9.11 \cdot 10^{-13}T^2 \\ &\quad - 1.5 \cdot 10^{-14}T^3\big) \\ &\cdot \big(1 - 3.83 \cdot 10^{-5}z + 4.9 \cdot 10^{-10}z^2\big). \end{aligned}$$

$T > 20\,°\mathrm{C}$

$$\begin{aligned} A_0 = &\big(3.964 \cdot 10^{-10} - 1.146 \cdot 10^{-11}T + 1.45 \cdot 10^{-13}T^2 \\ &\quad - 6.5 \cdot 10^{-16}T^3\big) \\ &\cdot \big(1 - 3.83 \cdot 10^{-5}z + 4.9 \cdot 10^{-10}z^2\big). \end{aligned}$$

Boric acid $B(OH)_3$ contribution:

$$\begin{aligned} A_1 &= \frac{8.86}{1412 + 3.21T + 1.19 \cdot 10^3 S + 1.67 \cdot 10^{-2}z} \\ &\quad \cdot 10^{(0.78pH - 8)}, \\ f_1 &= 2.8\sqrt{\frac{S}{3.5 \cdot 10^{-2}}}\,10^{\left(7 - \frac{1245}{T+273}\right)}. \end{aligned}$$

Sulfate of Magnesium Mg(SO)4 contribution:

$$\begin{aligned} A_2 &= \\ &\frac{21.44S(1+2.5 \cdot 10^{-2}T)(1-1.37 \cdot 10^{-4}z+6.2 \cdot 10^{-9}z^2)}{1412 + 3.21T + 1.19 \cdot 10^3 S + 1.67 \cdot 10^{-2}z}, \\ f_2 &= \frac{8.17 \cdot 10^{\left(11 - \frac{1990}{T+273}\right)}}{1 + 1.8(S - 3.5 \cdot 10^{-2})}. \end{aligned}$$

Acknowledgement

The authors wish to thank M. Brussieux for his assistance in obtaining the experimental data at the GESMA facilities. This work was partially supported by the Groupe d'Etudes Sous-Marine de l'Atlantique.

References

[1] P. J. Westervelt: Parametric acoustic array. J. Acoust Soc. Am. **35** (1963) 535–537.

[2] B. K. Novikov, O. V. Rudenko, V. I. Timoshenko: Nonlinear underwater acoustics. ASA translation book, 1987.

[3] M. F. Hamilton, D. T. Blackstock (eds.): Nonlinear acoustics. Academic Press, 1998.

[4] T. G. Muir, J. G. Willette: Parametric acoustic transmitting arrays. J. Acoust. Soc. Am. **52** (1972) 1481–1486.

[5] H. O. Berktay: Possible exploitation of non-linear acoustics in underwater transmitting applications. J. Sound and Vibration **2** (1965) 435.

[6] M. B. Moffett, R. H. Mellen: Model for parametric acoustic sources. J. Acoust. Soc. Am. **61** (1977) 325–337.

[7] M. B. Moffett, R. H. Mellen, W. L. Konrad: Parametric acoustic sources of rectangular aperture. J. Acoust. Soc. Am. **63** (1978) 1326–1331.

[8] M. F. Hamilton: Sound beams (Quasilinear theory). – In: Nonlinear Acoustics. M. F. Hamilton (ed.). Academic Press, 1998, Chap. 8 Part 3, 233.

[9] E. A. Zabolotskaya, R. V. Khokhlov: Quasi-plane waves in the nonlinear acoustics of confined beams. Sov. Phys. Acoust. **15** (1969).

[10] V. P. Kuznetsov: Equations of nonlinear acoustics. Sov. Phys. Acoust. **16** (1971) 467–470.

[11] J. Naze Tjotta, S. Tjotta, E. H. Vefring: Effect of focusing on the nonlinear interaction between two collinear finite amplitude sound beams. J. Acoust. Soc. Am. **89** (1991) 1017–1027.

[12] M. A. Averkiou, M. F. Hamilton: Nonlinear distorsion of short pulses radiated by plane and focused circular pistons. J. Acoust. Soc. Am. **102** (1997) 2539–2548.

[13] P. Alais, P.-Y. Hennion: Etude par une méthode de Fourier de l'interaction non linéaire de deux rayonnements acoustiques dans un milieu absorbant. Cas particulier de l'émission paramétrique. Acustica **43** (1979) 1–11.

[14] P. Alais, P.-Y. Hennion, P. Cervenka: Etude par analyse de Fourier des phénomènes non linéaires affectant la propagation ultrasonore dans un fluide. L'émission paramétrique. L'autodémodulation non linéaire. Revue de Physique Appliquée **20** (1985) 285–297.

[15] J. W. Goodman: Introduction to Fourier optics. McGraw-Hill, New-York, 1968.

[16] P. Alais: Effets de l'atténuation sur un rayonnement quelconque dans un milieu propagatif linéaire absorbant. Comptes-rendus de l'Académie des Sciences de Paris A **282** (1976) 547–549.

[17] J. Naze, S. Tjotta: Nonlinear interaction of two sound beams. J. Acoust. Soc. Am. **37** (1965) 174–175.

[18] P. Cervenka, P. Alais: Fourier formalism for describing non linear self-demodulation of primary narrow ultrasonic beam. J. Acoust. Soc. Am. **88** (1990) 473–481.

[19] J. R. Lovett: Merged seawater sound-speed equations. J. Acoust. Soc. Am. **63** (1978) 1713–1718.

[20] R. E. François, G. R. Garrison: Sound absorption based on ocean measurements. Part II: Boric acid contribution and equation for total absorption. J. Acoust. Soc. Am. **72** (1982) 1879–1890.

[21] G. S. Garrett, J. Naze Tjotta, S. Tjotta: Nearfield of a large acoustic transducer. Part I: Linear radiation. J. Acoust. Soc. Am. **72** (1982) 1056–1061.

[22] G. S. Garrett, J. Naze Tjotta, S. Tjotta: Nearfield of a large acoustic transducer. Part II: Parametric radiation. J. Acoust. Soc. Am. **74** (1983) 1013–1020.

[23] G. S. Garrett, J. Naze Tjotta, S. Tjotta: Nearfield of a large acoustic transducer. Part III: General results. J. Acoust. Soc. Am. **75** (1984) 769–779.

[24] J. Marchal, P. Cervenka: Nearfield of parametric transmission with finite-amplitude primary beams: Comparison between theoretical and experimental results. – In: 15th International Symposium on Nonlinear Acoustics, Göttingen, Germany, 1999; Nonlinear Acoustics at the turn of the Millennium. W. Lauterborn, T. Kurz (eds.). AIP, Melville, New York, 2000, 195–198.

[25] J. Naze Tjotta, S. Tjotta: Nonlinear interaction of two collinear, spherically spreading sound beams. J. Acoust. Soc. Am. **67** (1980) 484–490.

[26] J. Naze Tjotta, S. Tjotta: An analytical model for the nearfield of a baffled piston transducer. J. Acoust. Soc. Am. **68** (1980) 334–339.

[27] J. Naze Tjotta, S. Tjotta: Nonlinear equations of acoustics, with application to parametric acoustic arrays. J. Acoust. Soc. Am. **69** (1981) 1644–1652.

[28] P. Cervenka, P. Alais: Optimisation of a parametric transmitting array: Theoretical expression of the secondary field generated by finite amplitude narrow primary beams, using a Fourier analysis. Numerical charts at 15 kHz. – In: Frontiers of Nonlinear Acoustics. M. F. Hamilton (ed.). Elvesier Applied Science, London and New York, 1990, 233–238.